

Ultimate position resolution of pixel clusters with binary readout for particle tracking

Fuyue Wang^{1,2}, Benjamin Nachman², and Maurice Garcia-Sciveres²

¹*Department of Engineering Physics, Tsinghua University, Key Laboratory of Particle and Radiation Imaging, Ministry of Education, Beijing 100084, China*

²*Physics Division, Lawrence Berkeley National Laboratory, Berkeley, CA 94704, USA*

September 1, 2022

Abstract

Silicon tracking detectors can record the charge in each channel (analog or digitized) or have only binary readout (hit or no hit). While there is significant literature on the position resolution obtained from interpolation of charge measurements, a comprehensive study of the resolution obtainable with binary readout is lacking. It is commonly assumed that the binary resolution is $\text{pitch}/\sqrt{12}$, but this is generally a worst case upper limit. In this paper we study, using simulation, the best achievable resolution for minimum ionizing particles in binary readout pixels. A wide range of incident angles and pixel sizes are simulated with a standalone code, using the Bichsel model for charge deposition. The results show how the resolution depends on angles and sensor geometry. Until the pixel pitch becomes so small as to be comparable to the distance between energy deposits in silicon, the resolution is always better, and in some cases much better, than $\text{pitch}/\sqrt{12}$.

1 Introduction

The spatial resolution of silicon strip and pixel detectors has been analyzed in detail before (see for example [1–3]). This prior work has focused on the resolution that can be obtained by interpolation of charge measurements in adjacent channels, on the charge deposition and transport processes, on signal to noise of the charge measurement, and on functional forms to calculate position from measured charges. However, the resolution limits in the case of binary readout (no charge information, just hit or no hit above a preset threshold) have not been fully explored. For example, it is commonly stated that a single channel hit has a spatial resolution of $\text{pitch}/\sqrt{12}$ – the standard deviation of a uniform random variable on the interval $[0, \text{pitch}]$, but this is actually a worst case upper limit. Worst case means that no additional knowledge about the hit has been used, such as the observed cluster distributions in the detector that the hit belongs to, or the approximate incidence angles of the particle track producing the hit. Yet both of these things are known in practical applications, when

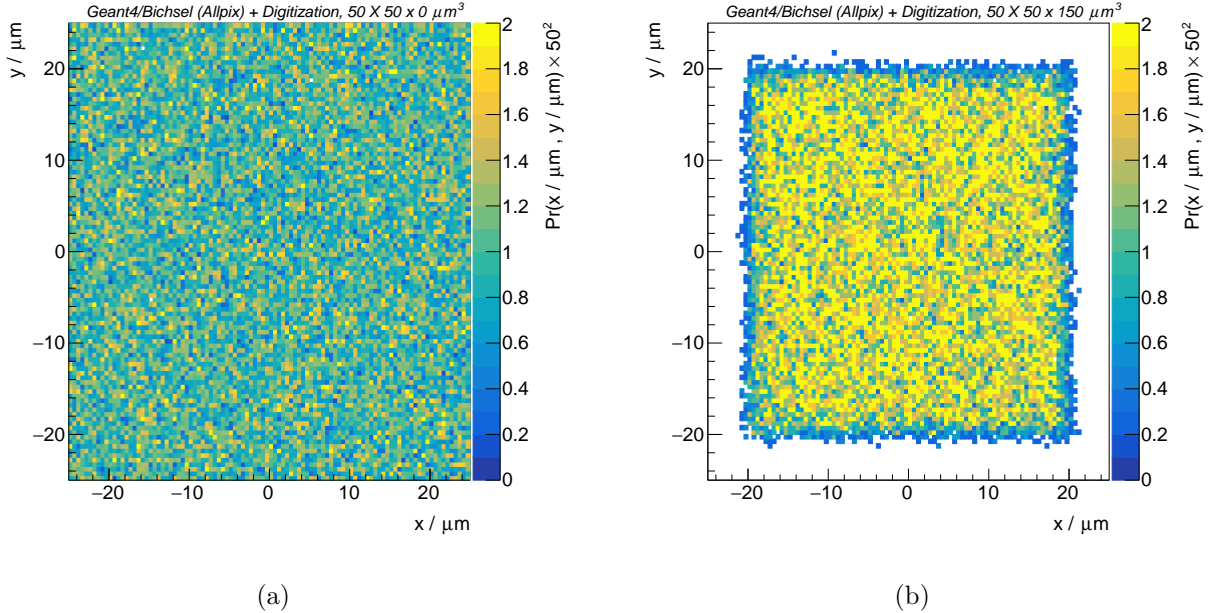


Figure 1: . Distribution of track positions in a single pixel cluster: (a) commonly assumed, which is only correct for an infinitely thin sensor; (b) actual for normal incidence tracks in a $50 \times 50 \times 150 \mu\text{m}^3$ sensor.

fitting a track to a collection of hits. For example, Fig. 1(a) shows the assumed hypothetical distribution of true track position in a pixel that leads to the $\text{pitch}/\sqrt{12}$ result, compared to the actual distribution in Fig. 1(b) of track positions for the case of single hit clusters in a $50 \times 50 \times 150 \mu\text{m}^3$ pixel sensor being crossed at normal incidence¹. The RMS of the actual distribution shown is $0.78 \times \text{pitch}/\sqrt{12}$. The reason is that tracks near the edge of the pixel will produce 2-pixel clusters instead of 1-pixel clusters. This charge sharing is related to the sensor thickness: in an infinitely thin sensor the track positions for 1-hit clusters would actually look like Fig. 1(a). The beneficial effect of knowing the cluster size distribution becomes greater for larger clusters, as will be seen later.

The goal of this paper is to survey the position resolution of binary readout pixels for a variety of pixel sizes of current and future interest, as shown in Table 1. We use a stand-alone simulation of a single pixel module to generate, for each sample, cluster distributions as a function of polar and azimuthal incidence angles in the range $0 < |\eta| < 3$ and $0 < \phi < 50^\circ$. The coordinates used are defined in Fig. 2. The pseudorapidity $\eta \equiv -\ln(\tan(\theta/2))$, where θ is the actual polar angle. The details of the simulation are presented in Sec. 2.

¹We present all results in the absence of a magnetic field. If a magnetic field is present the incidence angles relative to the sensor plane must be replaced by angles relative to the charge drift direction. The equivalent of “normal incidence” would thus be “parallel to the drift direction”.

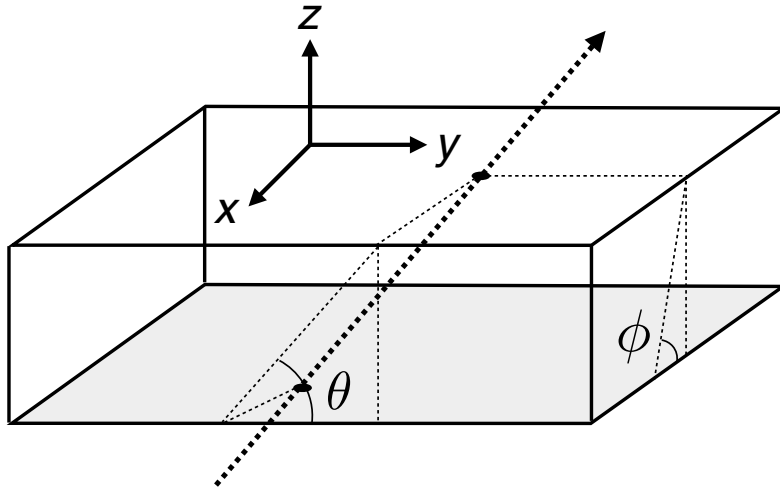


Figure 2: Definition of coordinates and incidence angles. The particle trajectory is shown as the heavy dotted line, with the sensor entrance and exit points marked by ovals.

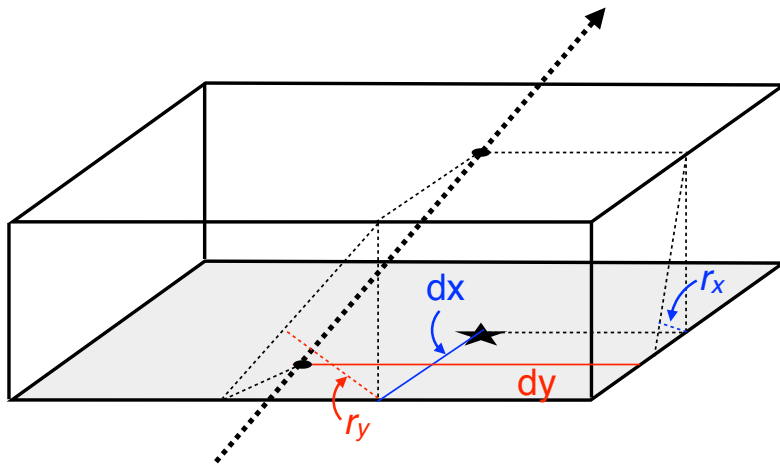


Figure 3: Definition of residual projections: r_x is the residual projection onto the x - z plane while r_y is the residual projection onto the y - z plane. The estimated entrance point is indicated by a star, while the true entrance and exit points are marked by ovals. The separations between estimated and true entrance points on the plane of the sensor surface, dx and dy , are also shown.

Pixel dimension	Sensor Thickness
$250\ \mu\text{m} \times 50\ \mu\text{m}$	$200\ \mu\text{m}$
$50\ \mu\text{m} \times 50\ \mu\text{m}$	$150\ \mu\text{m}, 100\ \mu\text{m}$
$100\ \mu\text{m} \times 25\ \mu\text{m}$	$150\ \mu\text{m}, 100\ \mu\text{m}$
$25\ \mu\text{m} \times 25\ \mu\text{m}$	$100\ \mu\text{m}, 50\ \mu\text{m}$
$10\ \mu\text{m} \times 10\ \mu\text{m}$	$50\ \mu\text{m}, 20\ \mu\text{m}$
$5\ \mu\text{m} \times 5\ \mu\text{m}$	$20\ \mu\text{m}, 10\ \mu\text{m}$
$2\ \mu\text{m} \times 2\ \mu\text{m}$	$10\ \mu\text{m}, 5\ \mu\text{m}$

Table 1: Simulated pixel sensor geometries.

2 Simulation

The simulation is based on the Geant4 package [4]. We are concerned with intrinsic resolution for minimum ionizing charged particles and therefore simulate a monochromatic source of 20 GeV muons. For low momentum particles, the hit residuals will be dominated by multiple scattering, and therefore this analysis is mainly of interest to relatively high momentum particles. Since the incidence angle will not be perfectly known when fitting a collection of hits, we uniformly smear the entrance angles in each simulation by 1 mrad. In terms of multiple scattering of 20 GeV muons, the RMS scattering angle when traversing 3% of a radiation length is about 0.1 mrad, which shows that the applied smearing is indeed coarse [5]. To ensure uniform illumination over at least one pixel, the source position is smeared uniformly by the pixel dimensions.

We simulate a single sensor at a time illuminated by the above source, with a variety of sensor thicknesses and pixel sizes as shown in Table 1. Only planar sensor geometry was simulated. We simulate collection of electrons. We use the Bichsel model [6] to predict the energy loss along the particle trajectory, and we convert the energy loss to charge via $1e^- = 3.6\ \text{eV}$. For computational convenience we quantize the charge in a number of electron clumps of order 10 per pixel pitch, except for the smallest pixels simulated, for which the number of electrons per pixel pitch is already of order 10 and no clumping is needed (each electron is its own clump). Each clump is transported to the sensor surface assuming drift along the electric field plus diffusion perpendicular to the field equal to $2.5\ \mu\text{m} \times \sqrt{d/300\ \mu\text{m}}$, where d is the drift length. This is the diffusion length expected at -10°C with $1\ \text{V}/\mu\text{m}$ field. We assume a uniform drift field of $1\ \text{V}/\mu\text{m}$ in all cases, which is above unirradiated depletion voltage for all thicknesses considered and is also consistent with saturation drift velocity [9].

The total charge arriving at each pixel is then compared to a threshold and the pixel is considered hit if the charge is above threshold, not hit otherwise. We use a threshold value of $1000\ e^-$ for $150\ \mu\text{m}$ thick sensors and scale it linearly with sensor thickness. We did not add an electronic noise contribution or a readout chip capacitive coupling-induced charge sharing as we are evaluating sensor resolution limits.

3 Shape Classification and RMS Calculation

For each incidence angle we observe several distinct cluster shapes and for each shape we record the distribution of particle track entrance points to the sensor. The optimal position estimator of each module given the shape and incidence angle is the mean of the entrance point distribution (the estimator that minimizes the mean squared error relative to the true position). Symbolically, the optimal position resolution is described by

$$\sigma_{\min}^2(x) \equiv \min (dx)^2 = \sum_{\text{shapes } s} \text{Pr}(s) \min (dx_s)^2 = \sum_{\text{shapes } s} \text{Pr}(s) \langle (x_{\text{true}} - \langle x_{\text{true}}|s \rangle)^2 \rangle, \quad (1)$$

where dx is defined in Fig. 3, $\text{Pr}(s)$ is the probability of a particular shape s , dx_s is conditioned on this shape s , and $\langle x_{\text{true}}|s \rangle$ is the average true entrance position given the shape s . An analogous formula describes the optimal position resolution in the y direction. As a consequence of Eq. 1, all that is needed to compute the optimal resolution is the RMS of the true position for all possible shapes. Since our pixel information is binary, two clusters with the same hit pixel pattern are indistinguishable. We histogram the true entrance point independently for each cluster shape and compute the mean and RMS of the distribution. As an example, Fig. 4 (a) shows the true entrance point y coordinate histogram for the cluster shape shown in (b). All position resolution results are shown normalized to the pitch/ $\sqrt{12}$ assumption.

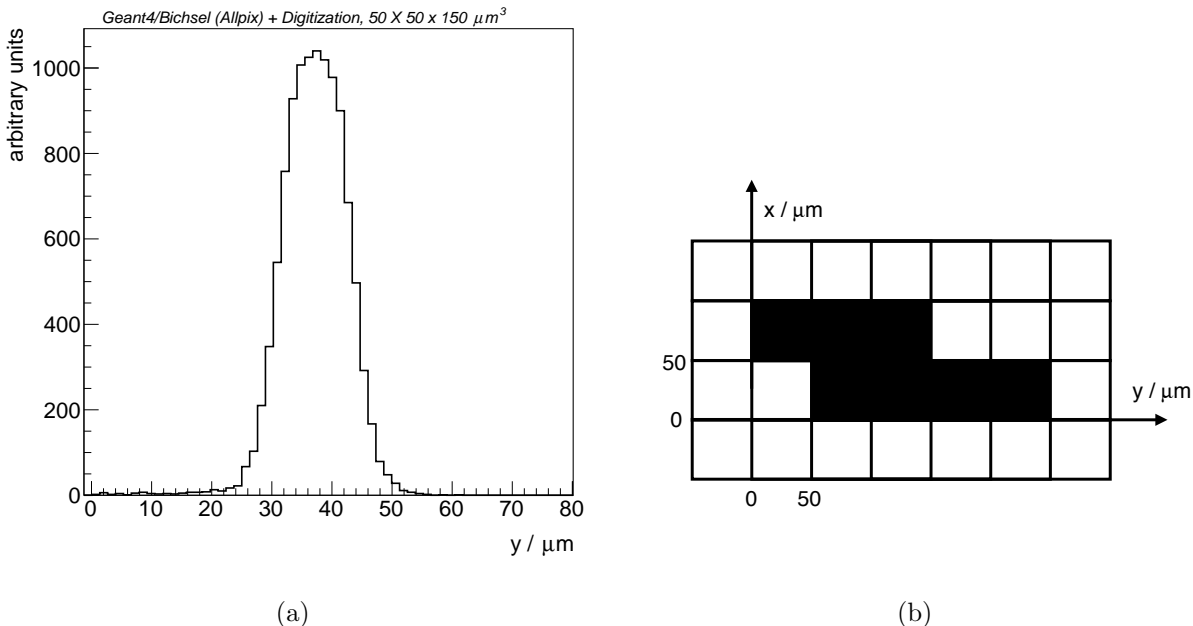


Figure 4: Histogram of entrance point y -coordinate (a) from all the clusters with the shape shown in (b). From simulation of $50 \times 50 \times 150 \mu\text{m}^3$ sensor with incidence angle $\phi = 10^\circ$, $|\eta| = 1.0$

Enumeration of all possible cluster shapes is not practical. We therefore do not worry in advance about how many different shapes will be generated. We process all simulated events

and simply create a new entrance point histogram for each new cluster shape that appears. The procedure is as follows:

1. Simulate a new event.
2. Check if an identical cluster shape has already occurred by comparing cluster to all existing histogram labels:
 - (a) If the shape matches an existing label, add entrance point to that existing histogram;
 - (b) If there is no match, create new histogram, label it with the cluster shape, and add entrance point to this histogram.

Two clusters are considered identical if they can be translated along x and y to lie exactly on top of each other, matching pixel-by-pixel. We do not consider rotations or reflections to produce a match. Furthermore, if $\text{Pr}(s)$ is small, then the contribution to Eq. 1 is negligible. We therefore only include in the calculation of σ_{\min}^2 those histograms with at least 10 entries, which means that shape occurred at least 10 times in our simulation sample ($\text{Pr}(s) \approx 0.1\%$). The number of included cluster shapes can be seen in Table 2.

	$\phi = 0$	$\phi = 10^\circ$	$\phi = 20^\circ$	$\phi = 30$	$\phi = 40^\circ$	$\phi = 50^\circ$
$\eta = 0$	8	8	9	16	23	33
$\eta = 0.4$	11	13	12	18	26	34
$\eta = 0.8$	26	18	22	27	39	43
$\eta = 1.2$	50	33	34	43	54	73
$\eta = 1.6$	108	42	45	51	64	121
$\eta = 2.0$	104	68	71	92	109	187

Table 2: Number of cluster shapes occurring at least 10 times in our simulation for given incidence angles, for the $50 \times 50 \times 150 \mu\text{m}^3$ sensor.

4 Results

The position resolution of the binary readout depends on the variety of cluster shapes, which in turn depends on the incidence angle. Put another way, the resolution should be best when the maximum value of $\text{Pr}(s)$ is small. This relationship is quantified by Fig. 5, which shows the probability of that most popular shape and the optimal position resolution in the plane of ϕ vs. η incidence angles, for a $50 \times 50 \times 150 \mu\text{m}^3$ pixel sensor. As expected, regions of high(low) probability for the most probable shape correspond to a worse(better) position resolution and vice versa. Since for this angular range Fig. 5(left) is nearly symmetric about $\phi = \eta$, the x position resolution plot is similar to Fig. 5(right) with the ϕ and η axis labels swapped.

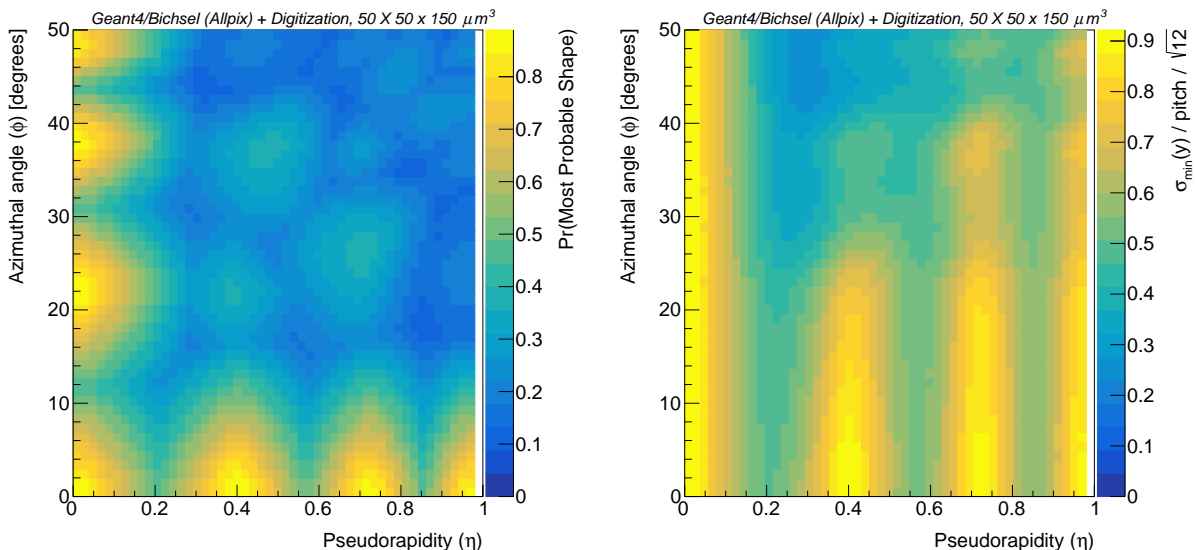


Figure 5: Left: The probability of the most frequent cluster shape for each ϕ and η angle combination (maximum $\text{Pr}(s)$). Right: the optimal y position resolution ($\sigma_{\min}(y)$).

The periodic structure in Fig. 5 is a result of the pixelated geometry. For a certain incidence angle represented by the red arrow in Fig. 6, no matter where along a pixel the particle enters the sensor, the MIP will always traverse two pixels. Due to diffusion and threshold effects, the number of hit pixels could be one or three with a small probability. The situation is different for an incidence angle represented by the black arrow in Fig. 6. When the particle enters to the left of the black arrow the cluster length will most likely be one pixel, while when the particle enters to the right the length will most likely be two pixels. Therefore, the chances of length = 1 and length = 2 are the same, so the probability of the most probable length (MPL) is near 50%. The full relationship between MPL and $|\eta|$ for $\phi = 0$ is shown in Fig. 7. The black arrow in Fig. 6 results in the first valley in Fig. 7 while the red arrow in Fig. 6 leads to the second peak in Fig. 7. Peak and valley positions in Fig. 7 repeat and approximately correspond to $\tan(\alpha_{\text{peak}}) = np/d$ and $\tan(\alpha_{\text{valley}}) = (n - 0.5)p/d$, where α is the incidence angle in a given direction, n is any positive integer, p is the pixel pitch, and d is the sensor thickness. The upper and lower bold lines in Figure 7 connect such

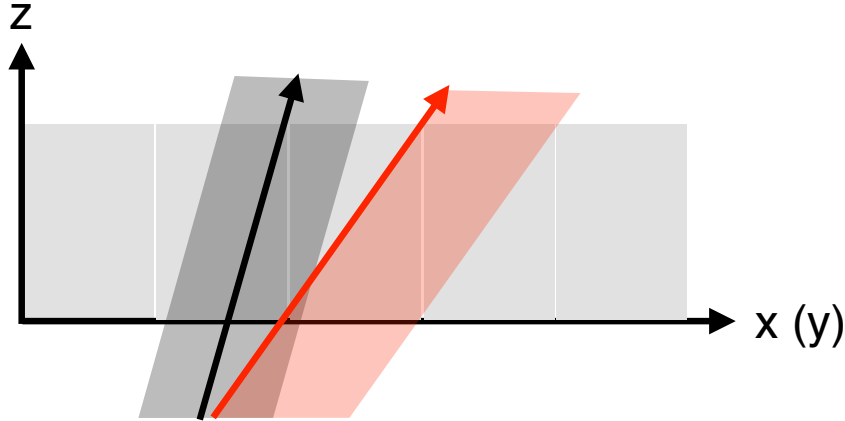


Figure 6: A sideways view of the pixel detector with arrows corresponding to possible MIP trajectories. The shaded red and black regions correspond to horizontal shifts of the arrows. The incidence angle of the black arrow is shallow enough to traverse either one or two pixels depending on its horizontal position. However, the red arrow will always traverse two pixels, no matter how it is translated horizontally.

peak and valley points, respectively.

In what follows we determine the position resolutions for the peak and valley points using the cluster shape classification method described in Sec. 3 as these resolutions provide upper and lower bounds, respectively. Resolutions for the x and y directions are analyzed separately. Since our simulation setup is symmetric, in principle x and y are interchangeable, but the angular ranges explored in the two directions are different. In the x direction we only go up to 50° incidence angle (where 0 is normal incidence), which is equivalent to $|\eta| \approx 1$, while in the y direction we scan up to $|\eta| = 2$, which is rather shallow incidence (84°). As we will show, shallow incidence angles result in rather different resolutions along and transverse to the incidence direction.

4.1 Resolution in the y direction

Fig. 8(a) shows the optimal y position resolution ($\sigma_{\min}(y)$) normalized to $\text{pitch}/\sqrt{12}$ for $50 \times 50 \times 150 \mu\text{m}^3$ pixels and $\phi = 0$ (normal incidence in the x direction). Points with a maximum (peak) or minimum (valley) in the probability of the most probable single cluster length are connected with a line. As described in the previous section, the most probable length is mostly responsible for the structure as a function of $|\eta|$ and therefore sets the resolution envelope. Points for a few arbitrary incidence angles are also shown to confirm that they lie within the envelope. Fig. 8(b) shows the resolution envelopes for different ϕ values (the incidence angle in the x direction). The resolution is almost always below 90% of $\text{pitch}/\sqrt{12}$ across the entire $|\eta|$ range probed. At small $|\eta|$ and large ϕ , the most probable length in the y direction becomes less relevant for setting the resolution boundaries because the shape in the x direction dominates the entrance position. Such extreme azimuthal incidence angles are not common in commonly implemented pixel detector layouts.

The optimal y position resolutions for all the sensor geometries of Table 1 are shown in

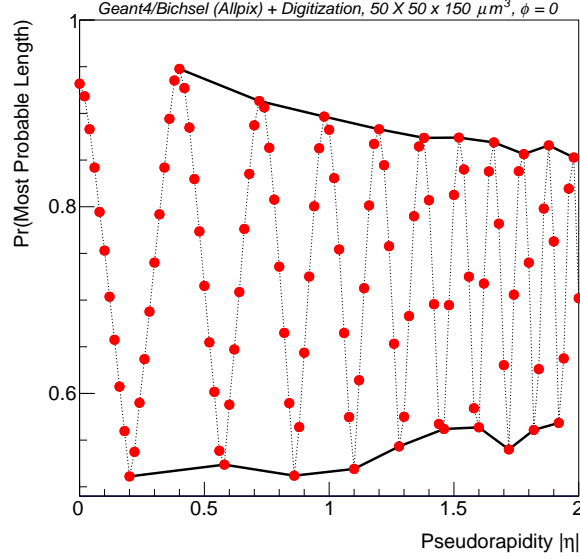


Figure 7: The probability of MPL as a function of $|\eta|$ for $\phi = 0$ and a $50 \times 50 \times 150 \mu\text{m}^3$ pixel sensor. The scatter seen at large incidence angles is statistical, as the $\text{Pr}(\text{MPL})$ values were determined from the simulation.

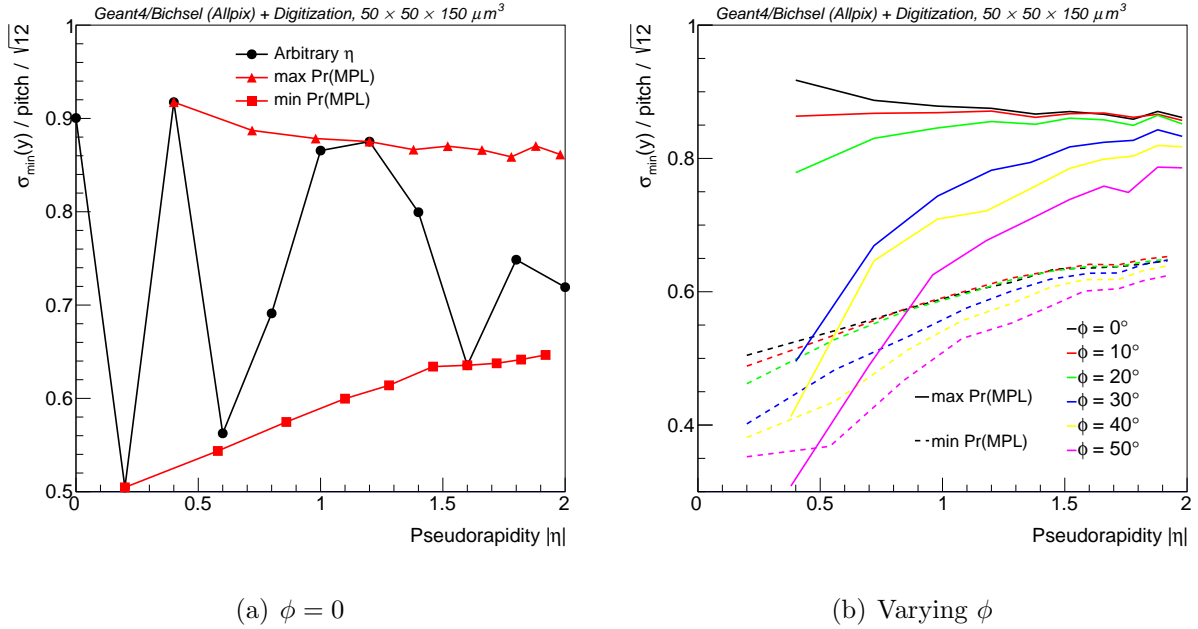
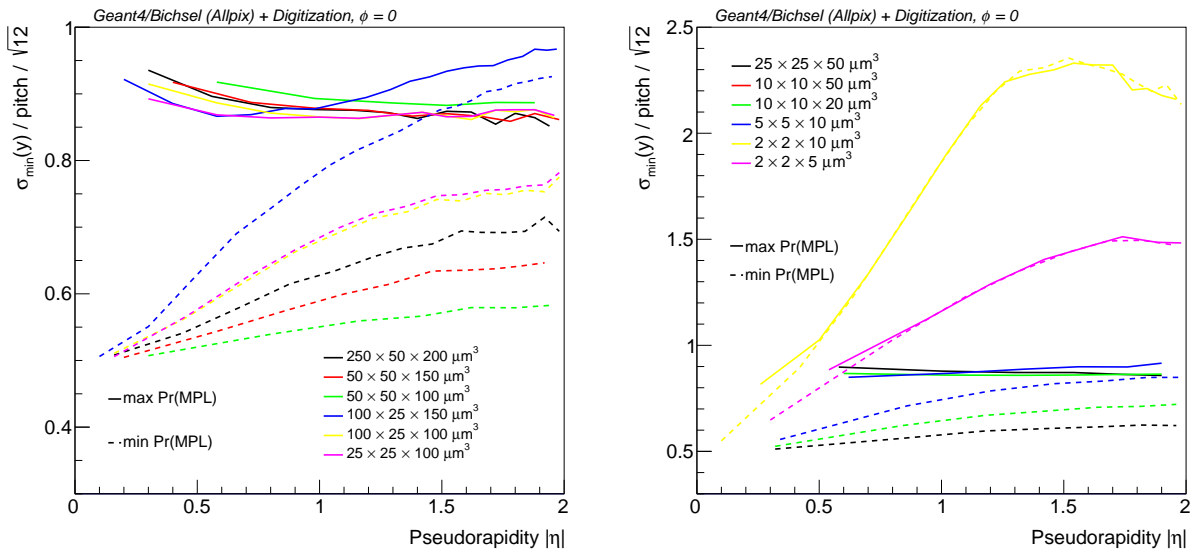


Figure 8: The optimal y position resolution normalized to $\text{pitch}/\sqrt{12}$ vs. $|\eta|$ for a $50 \times 50 \times 150 \mu\text{m}^3$ pixel sensor. The envelope of peak and valley points is shown by solid/dashed lines. (a) For $\phi = 0$, including a selection of arbitrary $|\eta|$ incidence angles, and (b) for different ϕ values.

Fig. 9, where the sensors have been divided into larger pixel sizes (Fig. 9(a)) and smaller pixel sizes (Fig. 9(b)). As before, the points corresponding to the peak and valley of the

Pr(MPL) distribution are connected with lines to illustrate resolution envelopes. For the larger pixels, there is little dependence on the size or $|\eta|$ for the peak resolution, which is around 90% of $\text{pitch}/\sqrt{12}$ for all sensor geometries. The lower bound for the large pixels depends strongly on the size and $|\eta|$, with the biggest angle dependence for the smaller y -pitch sensors. For the small pixel sizes, both the upper and lower Pr(MPL) envelopes depend strongly on $|\eta|$ and the resolution can even exceed $\text{pitch}/\sqrt{12}$. This happens when the charge deposition in the head or tail pixel is below threshold. For very small path lengths, there is a non-negligible probability that the MIP will traverse a pixel without leaving any charge. The average distance between energy depositions in the $2 \times 2 \times 5 \mu\text{m}^3$ is about $0.25 \mu\text{m}$. Diffusion compounds this 'ionization statistics' problem, resulting in worse resolution for the $10 \mu\text{m}$ thick sensor.



(a) Large pixel size in y direction

(b) Small pixel size in y direction

Figure 9: The optimal y position resolution normalized to $\text{pitch}/\sqrt{12}$ vs. $|\eta|$ (with $\phi = 0$ for (a) larger pixel sizes and (b) smaller pixel sizes). The envelope of peak and valley points is shown by solid/dashed lines.

4.2 Resolution in the x direction

Figure 10 shows the optimal x position resolution normalized to $\text{pitch}/\sqrt{12}$ as a function of $|\eta|$. Except for the curve at $\phi = 0$, the other lines correspond to the minima and maxima of Pr(MPL) for MPL in the x direction. It is clear that a detector geometry assuring a non-zero ϕ incidence will benefit from a significant gain from the longer cluster-size as $|\eta|$ increases. At $\phi=0$, the resolution does not change with η in the range $|\eta| < 2$, which corresponds to length less than 11. With such cluster length one cannot resolve charge sharing of less than $\sim 10\%$ and for $\phi=0$ this only occurs when the track is very close to the pixel edges. The reason it is the same for both angles is because even though the cluster length is longer at

$|\eta| = 2$, the traversed silicon path length per pixel decreases². There is an increase in the x -axis cluster size when the pitch and depth are the same.

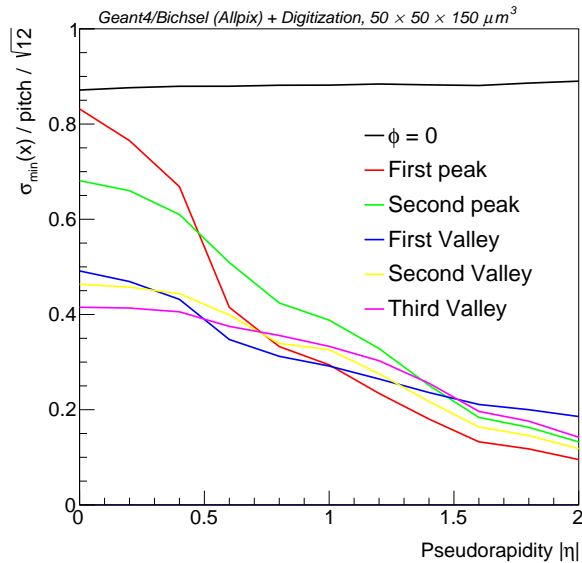


Figure 10: The optimal x position resolution normalized to $\text{pitch}/\sqrt{12}$ vs. $|\eta|$ at $\phi = 0$ and for various ϕ that correspond to the minima of $\text{Pr}(\text{MPL})$ for MPL in the x direction.

²The total number of off-axis pixels is higher at $|\eta| = 2$ even if the probability for at least one off-axis pixel is the same. More off-axis pixels should help to determine the position, but the low probability of any off-axis pixel significantly reduces any possible gains.

5 Conclusions

We have presented a comprehensive study of the pixel detector position resolution obtainable with binary readout. The results show how the resolution depends on angles and sensor geometry. Until the pixel pitch becomes so small as to be comparable to the distance between energy deposits in silicon, the resolution is always better, and in some cases much better, than the commonly assumed $\text{pitch}/\sqrt{12}$. This information can be of practical use for charged particle track fitting and design of new detectors. This work is particularly relevant for proposals at future experiments to have ultra small pixel detectors. So long as there are enough cluster shapes produced with significant probability, binary readout can already be powerful without the need for additional charge information.

6 Acknowledgments

This work was supported by the U.S. Department of Energy, Office of Science under contract DE-AC02-05CH11231 and by the China Scholarship Council.

References

- [1] R. Gluckstern, Uncertainties in track momentum and direction, due to multiple scattering and measurement errors 24 (1963) 381.
- [2] R. Turchetta, Spatial resolution of silicon microstrip detectors 335 (1993) 44–58. doi:[10.1016/0168-9002\(93\)90255-G](https://doi.org/10.1016/0168-9002(93)90255-G).
- [3] M. Boronat, et al., Physical limitations to the spatial resolution of solid-state detectors, IEEE Trans. Nucl. Sci. 62 (1) (2015) 381–386. arXiv:[1404.4535](https://arxiv.org/abs/1404.4535), doi:[10.1109/TNS.2014.2376941](https://doi.org/10.1109/TNS.2014.2376941).
- [4] GEANT4 Collaboration, GEANT4: A Simulation toolkit, Nucl. Instrum. Meth. A506 (2003) 250–303.
- [5] C. Patrignani, et al., Review of Particle Physics, Chin. Phys. C40 (10) (2016) 100001. doi:[10.1088/1674-1137/40/10/100001](https://doi.org/10.1088/1674-1137/40/10/100001).
- [6] H. Bichsel, Straggling in Thin Silicon Detectors, Rev. Mod. Phys. 60 (1988) 663–699. doi:[10.1103/RevModPhys.60.663](https://doi.org/10.1103/RevModPhys.60.663).
- [7] Q. Zeng, Search of New Physics with Boosted Higgs Boson in Hadronic Final States with ATLAS Detector, Stanford PhD Thesis (2017) [purl.stanford.edu/kt719mz9192].
- [8] F. Wang, B. Nachman, M. Garcia-Sciveres, The Impact of Incorporating Shell-corrections to Energy Loss in Silicon, In Preparation.
- [9] C. Jacoboni, et al., A review of some charge transport properties of silicon, Solid-State Electronics 20 (1977) 77 – 89. doi:[http://dx.doi.org/10.1016/0038-1101\(77\)](http://dx.doi.org/10.1016/0038-1101(77))

90054-5.

URL <http://www.sciencedirect.com/science/article/pii/0038110177900545>